A practical spectral method for hyperbolic conservation laws

Yu-Hui Sun[1], Y. C. Zhou[1] and G. W. Wei[1,2*]

[1] *Department of Mathematics, Michigan State University, East Lansing, MI 48824*

[2] *Department of Computational Science, National University of Singapore, Singapore 117543*

Abstract

A class of high-order lowpass filters, the discrete singular convolution (DSC) filters, is utilized to facilitate the Fourier pseudospectral method for the solution of hyperbolic conservation law systems. The DSC filters are implemented directly in the Fourier domain (i.e., windowed Fourier pseudospectral method), while a physical domain algorithm is also given to enable the treatment of some special boundary conditions. By adjusting the effective wavenumber region of the DSC filter, the Gibbs oscillations can be removed effectively while the high resolution feature of the spectral method can be retained. The utility and effectiveness of the present approach is validated by extensive numerical experiments.

Key words: Hyperbolic conservation laws; Fourier pseudospectral method; Discrete singular convolution filters; Gibbs oscillations

*Corresponding author, wei@math.msu.edu

I. INTRODUCTION

It is well known that due to their accuracy and efficiency, spectral methods have great advantages over local methods in solving applicable scientific and engineering problems [4,7,10,12,39]. Given a hyperbolic system of nonlinear conservation laws

$$\mathbf{u}_t + \mathbf{f}(\mathbf{u})_x = 0, \tag{1}$$

with initial condition

$$\mathbf{u}(x, 0) = \mathbf{u}_0(x), \tag{2}$$

its solution may not exist in the classical sense because of possible discontinuities. The direct use of spectral methods to this problem will encounter the Gibbs oscillations [16], which lead to blow-up in the time integration. Therefore, it has been of great interest in making spectral methods applicable to the hyperbolic conservation law systems in the past two decades. The expectation, as point out by Gottlieb [15], is that the use of spectral methods will enable us not merely to capture the shock, but also to capture the delicate features and structures of the flow. Obviously, spectral approaches will be extremely valuable to a class of aerodynamical problems that involve the interaction of both turbulence and shock [31]. Such an interaction is some of the most challenging problems in computation fluid dynamics.

The main objective of previous studies is to recover smooth solutions from those that are contaminated by Gibbs oscillations and, meanwhile, to improve the rate of convergence. For shock-capturing, many up-to-date local methods, such as weighted essentially non-oscillatory (WENO) scheme [29,35,36], central schemes [3,25,30,34], arbitrary-order non-oscillatory advection scheme [38], Gas kinetic [47], and image processing based schemes [18,44], perform well. The success of these local shock-capturing schemes lies in their appropriate amount of intrinsic numerical dissipation, which is introduced either by explicit artificial viscosity terms, or by upwinding, or by appropriate local average (non-oscillatory central schemes),

or by relaxation [24]. The characteristic decomposition based on Roe's mean matrix can also be considered as a local averaging on the Jacobian matrix $A(u) = \partial f(u)/\partial u$. In his recent work, LeVeque [28] outlined the relation between some approximate Riemann solvers and relaxation schemes. The relative amount of numerical dissipations may explain why the local characteristic decomposition is not necessary in low-order methods while it seems to be indispensable in high-order methods [35]. However, when these local methods are used in the cases where flow structures with fine details are needed to be resolved together with shocks, numerical dissipations are usually found to be so large that they smear the fine details [31]. The spectral methods, on the contrary, contribute very little numerical dissipation and dispersion in principle when used to approximate spatial derivatives. Nevertheless, when they are applied to the approximation of spatial derivatives on a domain containing discontinuities, the Gibbs oscillations again have to be suppressed by appropriate means, for which there are two general routines: (1) explicit artificial viscosity, e.g. spectral viscosity (SV) method proposed by Tadmor [37] and (2) filtering, which is the central issue of the present study.

At present, most filters are constructed in the spectral domain and they can be called spectral filters. Hussaini *et al.* [22] suggested a list of typical spectral filers, i.e. Lanzos filter, raised cosine filter, sharpened raised cosine filer and exponential cutoff filter. More sophisticate and effective filters in spectral domain are Vandeven's p-th order filter [40], Cai *et al.*'s sawtooth function [5] and Gottlieb and Tadmor's regularized Dirichlet function [13].

Apart from methods that are implemented in the spectral domain, filters in the physical domain are also developed. To design an appropriate filter in the physical domain is generally more difficult than in the Fourier domain. A straightforward procedure is to make use of numerical dissipation partially contained in *high-order* shock-capturing schemes [6], such as the ENO scheme, where, actually, numerical dissipations were introduced both in the Fourier domain (via an exponential filter) and in the physical domain (via ENO polynomial interpolation). Such a strategy was generalized by Yee *et al.* [49] to the so-called characteristic filter method (with finite difference or finite volume) which has been successfully

applied to shock-capturing and turbulence simulations. Another procedure was initiated by Gottlieb [14] by using the Gegenbauer polynomial to resolve the oscillatory partial Fourier summation. Some promising numerical results from the filter approach can be found in Refs. [8,9,17,21].

Nevertheless, some prominent issues may hinder the success of filtered spectral methods for practical numerical computations involving shocks. In our view, there are two very important issues that are vita to the success of a filtered spectral scheme. The first issue is how to select optimal filters for shock-capturing. The issue is very complex and cannot have a unique answer at this point because there are so many properties to mind, such as flatness, ripple, filter length, effective frequency range and length of transition band, to name only a few. Loosely speaking, it is desirable to have filters that are free of dispersion errors, flat while having very small transition band, short in length while having high resolution. Moreover, what adds to the complexity is that solutions to different hyperbolic conservation law systems may have different Fourier spectral distributions. Consequently, one faces the difficulty that an optimal filter for a problem may not even work for another one. Therefore, it is desirable to have a filter which accounts for this change by an adjustable parameter.

The second issue also concerns the change of solution, but is due to the time evolution for a given hyperbolic conservation law system. As the Fourier spectral distribution of a given problem changes with time, the question is how to implement the filter? It will be too dissipative for many systems if a filter is applied at each time step of the integration. Therefore, an adaptive implementation, which is controlled by a sensor during the time integration, is appropriate. Given the complexity, it is unlikely that there will be an ideal solution to these issues in the immediate future. Obviously, these challenging and interesting problems call for the further study of spectral filter approaches.

The objective of this work is to construct, analyze and implement a class of high-order lowpass filters which can be used either in the Fourier domain or in the physical domain. These filters are constructed within the framework of the discrete singular convolution (DSC) algorithm [41–43] and they are used to suppress Gibbs oscillations arising in the Fourier

pseudospectral method (FPM). Such lowpass filters have a wide effective wavenumber range that makes it possible to capture the fine flow structures, which is a desirable objective of spectral methods for hyperbolic conservation law systems. It is this effective wavenumber range that controls the resolution of the overall method. In our design, this effective range can be varied according to the resolution requirement by a parameter. Different DSC kernels have different magnitude responses and adjustability in the Fourier domain, which in turn influence the accuracy and resolution. The DSC filters used in this work were originally designed in a conjugate filter oscillation reduction (CFOR) [19,45,46] scheme. By 'conjugate filters' it means that the effective wavenumber range of the lowpass filter is largely overlapped with that of the highpass filter which is used for the approximation of spatial derivatives. The resulting Fourier domain algorithm is essentially a windowed Fourier pseudospectral method for shock-capturing.

The rest of this paper is organized as follows. In Section II, a brief introduction will be devoted to the construction of the DSC lowpass filters followed by a discussion of two types of implementations of these filters to spectral methods. Extensive numerical experiments are carried out in Section III, including Burgers' equation, shock-tube problems, shock-entropy wave interaction, shock-vortex interaction. The shock-capturing ability and the high resolution feature of the present method are addressed. Concluding remarks end this paper.

II. THEORY AND ALGORITHM

A. DSC lowpass filter

In the context of distribution theory, a singular convolution is defined by

$$f(x) = (T * \eta)(x) = \int_{-\infty}^{\infty} T(x-t)\eta(t)dt, \tag{3}$$

where $T(x)$ is a singular kernel and $\eta(x)$ is an element of the space of test functions. Interesting singular kernels include that of Hilbert type, Abel type and delta type. The former

two play important roles in the theory of analytical functions, processing of analytical signals, theory of linear responses and Radon transform. Since delta type kernels are the key element in the theory of approximation and the numerical solution of differential equations, we focus on singular kernels of the delta type

$$T(x) = \delta^{(q)}(x) \ , \ q = 0, 1, 2, \cdots \ , \tag{4}$$

where superscript (q) denotes the qth-order 'derivative' of the delta distribution $\delta(x)$, with respect to x, which should be understood as generalized derivatives of distributions. When $q = 0$, the kernel $T(x) = \delta(x)$ is important for the interpolation of functions. In this work, only the case of $q = 0$ will be involved. One has to find appropriate approximations to the above singular kernel, which can not be directly realized in computers. To this end, we consider a sequence of approximations

$$\lim_{\alpha \to \alpha_0} \delta_\alpha^{(q)}(x) = \delta^{(q)}(x) \ , \ q = 0, 1, 2, \cdots \tag{5}$$

where α is a parameter which characterizes the approximation with the α_0 being a generalized limit. Among various candidates of approximation kernels [42], regularized Shannon kernel (RSK)

$$\delta_{\sigma,\Delta}(x - x_k) = \frac{\sin \frac{\pi}{\Delta}(x - x_k)}{\frac{\pi}{\Delta}(x - x_k)} \exp\left(-\frac{(x - x_k)^2}{2\sigma^2}\right) \tag{6}$$

is frequently used due to its close link to the Shannon sampling theorem. In this formula, Δ is the grid spacing and σ determines the width of the Gaussian envelop. For a given $\sigma \neq 0$, the limit of $\Delta \to 0$ reproduces the delta kernel (distribution). With the RSK, a function u can be approximated by a discrete convolution

$$u(x) \approx \sum_{k=-W}^{W} \delta_{\sigma,\Delta}(x - x_k) u(x_k) \ , \ q = 0, 1, 2, \cdots \ , \tag{7}$$

where $\{x_k\}_{k=-W}^{W}$ are a set of discrete grid points which are centered at x, and $2W + 1$ is the computational bandwidth, or effective kernel support, which is usually smaller than the computational bandwidth of the spectral method - the entire domain span. Equation (7) is often referred as a DSC and the RSK is used as the prototype of a DSC lowpass filter.

The feasibility of the DSC-RSK as lowpass filters in numerical computation is based on an important observation: by adjusting the ratio r ($r = \frac{\sigma}{\Delta}$) of the regularizer, one can control the effective wavenumber region and thus, control the resolution of the lowpass filter. We plot the frequency response profile of the DSC-RSK lowpass filter in FIG. 1. A distinct property of the RSK lowpass filter is that there is no ripples in its passband; thus the application of this filter will not impart the low frequency. In contrast, some lowpass filters constructed with certain polynomials may have ripples in their passband, which would rule out their application to numerical integrations, especially for long time evolution, where the solution may be distorted after repeated filtering.

The maximum effective wavenumber (frequency) range of the DSC-RSK is determined by the ratio r, which in turn is determined by computational bandwidth W. The philosophy is simple since with the increase of W, the Gaussian window should also be enlarged to fully utilize the stencil. The optimal values r at different W can be estimated and they characterize the effective wavenumber range. The larger the optimal r is, the wider the effective wavenumber range will be. When r value is chosen larger than the optimal value for a given W, the accuracy of the resulting filter will be degraded by oscillations. Hence we do not recommend the use of r beyond the optimal value unless in some circumstances where the filer is utilized to stabilize a long-time integration.

B. Fourier domain algorithm

We denote $\zeta(x_j) = \delta_{\sigma,\Delta}(x_j)$ the proposed DSC-RSK lowpass filter in the physical domain $[0, L]$ and $\hat{\zeta}(\omega_n)$ its image in the Fourier domain, where $\Delta = L/N$, $x_j = j\Delta$ and $\omega_n = \frac{2\pi n}{L}$. The obvious relation between $\zeta(x_j)$ and $\hat{\zeta}(\omega_n)$ is

$$\hat{\zeta}(\omega_n) = \Delta \sum_{j=0}^{N-1} \zeta(x_j) e^{-i\omega_n x_j}. \tag{8}$$

As in the previous work [15], filtering in the Fourier domain is usually accomplished by multiplying the given Fourier coefficients $\hat{u}(\omega_n) = \Delta \sum_{j=0}^{N-1} u(x_j) e^{-i\omega_n x_j}$ by $\hat{\zeta}(\omega_n)$ directly, i.e., a windowed Fourier transform,

$$u^{\zeta}(x_j) = \frac{1}{L} \sum_{n=-\frac{N}{2}}^{\frac{N}{2}-1} \hat{\zeta}(\omega_n)\hat{u}(\omega_n)e^{i\omega_n x_j}. \tag{9}$$

Therefore, the *modified* Fourier coefficients $\hat{\zeta}(\omega_n)\hat{u}(\omega_n)$ in Eq. (9) are the Fourier coefficients of a *localized* version of the original function $u(x_j)$: $u^{\zeta}(x_j)$. Hence, errors arising from the discontinuity are also localized and the accuracy away from the discontinuity can be ensured. In practical applications, one only needs to carry out the filtering and differentiation $D_x u = u_x$ in one step

$$u_x^{\zeta}(x_j) = \frac{1}{L} \sum_{n=-\frac{N}{2}}^{\frac{N}{2}-1} i\omega_n\hat{\zeta}(\omega_n)\hat{u}(\omega_n)e^{i\omega_n x_j}. \tag{10}$$

A standard forth-order Runge-Kutta (RK-4) scheme is employed for the time advance scheme in this work. We use a TVD switch to adaptively activate the application of the DSC-RSK lowpass filter. Whenever the total variation of the approximate solution in the two consecutive time steps exceeds a prescribed criteria, the lowpass filter is activated. The DSC-RSK lowpass filter is only applied at the end of each full RK-4 cycle. The reader is referred to our earlier work [19,45,46] for the detail of this adaptive filtering.

C. Physical domain algorithm

It is more difficult to apply the filter in the physical domain than in the Fourier domain. On one hand, it is not easy to quantitatively analyze the influence of numerical dissipation in the physical domain. On the other hand, the convolution operation

$$u^{\zeta}(x) = \int u(x-\xi)\zeta(\xi)d\xi, \tag{11}$$

complicates the physical domain application of the filter. However, in some practical applications, it turns out to be quite necessary to implement the filter in the physical domain, especially for problems whose boundaries require some special treatments. The reflective boundary is one of such examples that need to be treated by using grid points outside the computational domain. In this work, we propose the method to apply our DSC-RSK lowpass

filter in the physical domain. Due to the fact that the RSK lowpass filter is an interpolatory kernel, we consider a two-step procedure. Step one is the prediction of mid-mesh values from the nodal values

$$u^{\zeta}_{i+\frac{1}{2}} = \sum_{j=-W}^{-1} u_{i+j+1}\zeta((j+\frac{1}{2})\Delta) + \sum_{j=1}^{W} u_{i+j}\zeta((j-\frac{1}{2})\Delta). \tag{12}$$

The other is the reconstruction of the nodal values from the mid-mesh values

$$u^{\zeta\zeta}_{i} = \sum_{j=-W}^{-1} u^{\zeta}_{i+j+\frac{1}{2}}\zeta((j+\frac{1}{2})\Delta) + \sum_{j=1}^{W} u^{\zeta}_{i+j-\frac{1}{2}}\zeta((j-\frac{1}{2})\Delta), \tag{13}$$

where, u_i denotes $u(x_i)$ and Δ is the grid spacing. The lowpass filter with a r value smaller than the optimal value is used in one of these two steps. The activation of the RSK lowpass filter is controlled in the same manner as that of the frequency domain algorithm.

As described, the DSC-RSK lowpass filter can be applied either in the physical domain or in the Fourier domain. In general, filtering in the Fourier domain is much easier and more convenient than in the physical domain because no additional summation is required to implement the filter in the Fourier spectral method. In contrast, the physical domain implementation requires two additional summations. Therefore, we have used the filter in the Fourier domain in most of our numerical experiments except for the cases in which the reflective boundary condition is involved. We have checked that whenever applicable, results obtained from the Fourier domain approach and the physical domain approach are identical.

D. Post processing filter

Once the time integration has been completed, a strong filter is usually required for post processing the solution so as to make the solution more presentable. In principle, we only need to reduce the r value of the DSC-RSK lowpass filter at the last time step of the computation. As an alternative, we provide a series of lowpass filters based on the Lagrange delta kernel which is given by

$$\delta_W(x, x_j) = \prod_{k=-W, k\neq j}^{W} \frac{x - x_k}{x_j - x_k}, \ j = -W, \cdots, W. \tag{14}$$

FIG. 2 shows the magnitude response of the Lagrange delta kernel. In fact, the highpass versions of these filters are graphically identical to centered finite difference (FD) schemes. In our numerical experiments, we adopt Lagrange-2 or Lagrange-4 as post processing filters. Their efficiency is demonstrated by our numerical results.

III. NUMERICAL EXPERIMENTS

In this section, we examine the validity and demonstrate the performance of proposed windowed (filtered) Fourier spectral scheme for conservation law systems. A large collection of standard linear and nonlinear benchmark problems [36], including the linear advection equation, 1D inviscid Burgers' equation, shock tube (Sod and Lax) problems, 1D shock-entropy interaction, 2D shock-entropy interaction, 2D shock-vortex interaction, 2D advection of an isentropic vortex and flow past a cylinder, are considered in the present study. Some of these problems have periodic boundary conditions therefore the windowed Fourier pseudospectral method will be applied directly. For problems whose boundary conditions are not periodic, we symmetrically double the computational domain in both x and y directions to compute the flux derivative. It is noted that the extension is necessary for constructing periodic problem feasible for the Fourier spectral method. Our filtering procedures, as described earlier, can be applied with general boundary conditions, such as Dirichlet or Neumann. In the appendix, we list the filter parameter r used for each numerical example.

A. Scalar conservation law systems

We begin our numerical experiments with the scalar conservation law system, which is given by

$$u_t + f(u)_x = 0, \tag{15}$$

where $f(u)$ is a function of u. It is generally believed that spectral methods are not very suitable for simple shock profiles and should not be used if one is interested primarily in the

shock profiles rather than other detailed structures of the flow. In this study, we choose scalar conservation law systems to illustrate that the proposed global spectral scheme performs well for a class of localized shock problems.

Example 1. We first solve a linear advection equation, which is of the form

$$\begin{aligned} u_t + u_x &= 0 \quad -1 < x < 1, \\ u(x,0) &= u_0(x) \quad \text{periodic}, \end{aligned} \tag{16}$$

where, u_0 is an initial value

$$u_0(x) = \begin{cases} \frac{1}{6}(G(x,\beta,z-\delta) + G(x,\beta,z+\delta) + 4G(x,\beta,z)) & -0.8 \le x \le -0.6 \\ 1 & -0.4 \le x \le -0.2 \\ 1 - |10(x-0.1)| & 0 \le x \le 0.2 \\ \frac{1}{6}(F(x,\alpha,a-\delta) + F(x,\alpha,a+\delta) + 4F(x,\alpha,a)) & 0.4 \le x \le 0.6 \\ 0 & \text{otherwise.} \end{cases} \tag{17}$$

Here, functions G and F are defined as

$$\begin{aligned} G(x,\beta,z) &= e^{-\beta(x-z)^2} \\ F(x,\alpha,a) &= \sqrt{\max(1-\alpha^2(x-a)^2, 0)}, \end{aligned} \tag{18}$$

where $a = 0.5$, $z = -0.7$, $\delta = 0.005$, $\alpha = 10$ and $\beta = \frac{\log 2}{36\delta^2}$.

The solution of this problem contains a combination of a Gaussian, a square wave, a sharp triangle wave and a half ellipse. The exact solution at any time can be easily obtained by a translation of the initial solution at speed 1. In FIG. 3 and FIG. 4, we display the numerical results for this problem at t=8 with 128 and 256 grid points, respectively. We observe that our method works well in both cases.

Example 2. Secondly, we test the proposed method by considering a moving W-shape wave, i.e., a piecewise continuous initial value, for the linear advection equation with an initial value [45]

$$u_0(x) = \begin{cases} 1 & 0 \le x \le 0.2 \\ 4x - \frac{3}{5} & 0.2 \le x \le 0.4 \\ -4x + \frac{13}{5} & 0.4 \le x \le 0.6 \\ 1 & 0.6 \le x \le 0.8 \\ 0 & \text{otherwise.} \end{cases} \tag{19}$$

This case is very similar to Example 1. It contains the so-called contact discontinuity and is quite difficult to solve in hyperbolic conservation laws. In particular, the interaction of two lines at $x = 0.2$ and $x = 0.6$ is difficult to resolve. Hence, it is a good test for the shock-capturing ability of the present method. We compute the solution up to t=8. The results are shown in FIG. 5 and FIG. 6.

Example 3. Having solved the linear equation with different initial values, we consider the solution of the most popular inviscid Burgers' equation, in which $f(u) = u^2/2$ and the Riemann type initial value is given by

$$u(x,0) = \begin{cases} 1 & x \le 0 \\ 0 & x > 0. \end{cases} \tag{20}$$

This is a standard benchmark problem in hyperbolic conservation laws and has been considered by numerous researchers. The exact solution is a shock wave with a constant velocity

$$u(x,t) = \begin{cases} 1 & x - St < 0 \\ 0 & x - St > 0, \end{cases} \tag{21}$$

where the speed of the shock front is

$$S = \frac{1}{2}. \tag{22}$$

We should note that this case is a non-periodic boundary problem. We must symmetrically double the computational domain in the x-direction when we calculate the derivative of the flux. This operation is necessary because it generates the periodic boundary condition so that the Fourier spectral method can be used. The numerical results are plotted in FIG. 7 at time t=2.

Example 4. Another Riemann type initial value for the inviscid Burgers' equation with a flux of $u^2/2$ is given by

$$u(x,0) = \begin{cases} 0 & x < 0 \\ 1 & x \geq 0. \end{cases} \tag{23}$$

The exact solution of this problem is a rarefaction wave

$$u(x,t) = \begin{cases} 0 & \frac{x}{t} < 0 \\ \frac{x}{t} & 0 < \frac{x}{t} < 1 \\ 1 & \frac{x}{t} > 1. \end{cases} \tag{24}$$

Numerical results are plotted in FIG. 8 at t=2 with different numbers of nodal points. Particularly, one can see that the end of the rarefaction fan is well resolved.

Example 5. Finally, we use non-convex flux to test the convergence to the physically correct solution. The flux is a non-convex function

$$f(u) = \frac{1}{4}(u^2 - 1)(u^2 - 4) \tag{25}$$

with a Riemann type initial value

$$u(x,0) = \begin{cases} -3 & x < 0 \\ 3 & x \geq 0. \end{cases} \tag{26}$$

The reader is referred to [20] for more detailed information about this problem. The results are displayed in FIG. 9 at t=0.04. Again, present spectral solver yields a satisfactory resolution.

B. Euler systems in one dimension

In this subsection, we perform numerical experiments by using the proposed scheme for the 1D Euler equation of gas dynamics. In one dimension, the Euler equation takes the form

$$U_t + F(U)_x = 0 \tag{27}$$

with

$$U = \begin{pmatrix} \rho \\ \rho u \\ E \end{pmatrix}; \quad F(U) = \begin{pmatrix} \rho u \\ \rho u^2 + p \\ u(E+p) \end{pmatrix}, \tag{28}$$

where, ρ, u, p and E denote the density, velocity, pressure and total energy per unit mass $E = \rho(e + (u^2)/2)$, respectively. Here, e is the specific internal energy. For an ideal gas with the constant specific heat ratio ($\gamma = 1.4$) considered here, one has $e = p/(\gamma - 1)\rho$. We consider the following two well-known Riemann problems.

Example 6. We solve for the solution of two shock tube problems with Sod's and Lax's initial conditions [23], i.e.,

$$(\rho, u, p)_{t=0} = \begin{cases} (1, 0, 1), & x < 0 \\ (0.125, 0, 0.1), & \text{otherwise} \end{cases} \tag{29}$$

for the Sod problem and

$$(\rho, u, p)_{t=0} = \begin{cases} (0.445, 0.698, 3.528), & x < 0 \\ (0.5, 0, 0.571), & \text{otherwise} \end{cases} \tag{30}$$

for the Lax problem. The numerical results for these two problems are shown in FIG. 10 and FIG. 11, respectively. We can see that the present method gives a good resolution in both cases. Similar to all the methods depending on the numerical dissipation, the resolution for the linear degenerate contact discontinuity is slightly lower than that for the generic nonlinear shock wave. If combined with Harten's artificial compression method, present spectral solver should have better resolution for the contact discontinuity.

Example 7. In this example, the interaction of an entropy wave of small amplitude with a Mach 3 right-moving shock in a one-dimensional flow is investigated. The computational domain is taken as $[0, 9]$ and the flow field is initialized with

$$(\rho, u, p)_{t=0} = \begin{cases} (3.85714, \quad 2.629369, \quad 10.33333) & x \leq 0.5 \\ (e^{-\epsilon \sin(\kappa x)}, \quad 0, \quad 1.0) & x > 0.5 \end{cases} \tag{31}$$

where ϵ and κ are the amplitude and the wave number of the entropy wave before the shock. This problem is significant due to its relevance to the interaction of shock-turbulence. Spectral methods, by nature of their high accuracy and negligible dispersive and dissipative errors, are ideally suited to the numerical study of turbulence and have already been widely applied. Here we would like to argue the feasibility of the present spectral method to the shock-turbulence interaction. In our test, we vary the wavenumber of the pre-shock wave while keeping its amplitude unchanged ($\epsilon = 0.01$). As the wavenumber increases, the problem becomes more and more challenging because the amplified high-frequency entropy waves after the shock are always mixed with spurious oscillations. As the wavenumber increases, it is very difficult to distinguish the high-frequency waves from the spurious oscillations. A low-order scheme may dramatically damp the transmitted high frequency waves. Even some popular high-order schemes also encounter the difficulty in preserving the amplitudes of the entropy waves due to their excessive dissipation with a given mesh size. Therefore, a successful shock-capturing method should be able to eliminate Gibbs' oscillation while capturing the shock and preserving the high-frequency entropy waves.

In our test, we let the shock move from $x = 0.5$ to $x = 8.5$. For the purpose of comparison with the previous results, we only give the results at the interval $[4.0, 9.0]$. Also, in order to discharge the transient waves due to the non-numerical initial shock profile, we plot the length of the amplified entropy waves in the same manner as that in Ref. [23]. Furthermore, we must point out two nontrivial remarks for the following cases with different κ. One is that we have replotted the final results in a denser grid, otherwise the bounded strip will not be fully spanned due to the fact that no enough grid values locate near all the peaks /valleys of the wave. Another is that we have used a local filter in order to eliminate the oscillations near the shock when we present final results after the computation.

First, we consider $\kappa = 13$. In this case, the computational domain is deployed with 513 grids points. Such a mesh is suitable for the Fourier spectral method. The numerical results of the amplitude of the entropy waves are shown in FIG. 12(a). It can be seen that the shock and the generated entropy waves are ideally captured. The entropy waves fully span the

strip bounded by two solid lines at ± 0.08690716, which show the amplitude of the amplified entropy waves predicted by the linear analysis. Since post-shock waves are monochromic, a simple calculation indicates the point per wavelength (PPW) value of these waves is 7.125. Such value is larger than the spectral resolution (PPW=2.0) but it is much smaller than that obtained by most shock-capturing schemes. The transmitted waves suffer the similar smearing as the contact waves. The shock wave, on the contrary, is self-repairable due to its compression nature. This observation verified that the numerical dissipation needed for shock-capturing will degrade the resolution of the spectral method. It also verified that this degradation can be isolated and alleviated by the DSC-RSK filter.

We next double the wave number κ up to 26. A mesh of 513 grid points is not enough for simultaneous shock capturing and high-frequency wave resolving. Therefore, we increase the mesh size to $N = 1025$ for this computation. The results for this case are presented in FIG. 12(b). It is seen that no obvious deterioration happens to the results and the resolution in the post-shock waves is still satisfactory. The fullness of the wave is comparable with that of $\kappa = 13$. But the first two post-shock waves have been slightly polluted.

When the wave number κ is increased to 39 and 52, we use 2049 grid points to resolve such high-frequency waves. FIG. 12(c) and FIG. 12(d) show the results of $\kappa = 39$ and $\kappa = 52$, respectively. The same PPW value 7.125 is maintained in this high-frequency case. The good resolution of the present method in simulating this 1D shock entropy interaction indicates that our scheme is capable of and efficient in distinguishing the high-frequency entropy waves from spurious oscillations.

Example 8. Results are now shown for the problem of Shu and Osher which also describes the interaction of an entropy sine wave with a Mach 3 right-moving shock. The computational domain is taken as $[-1, 1]$ and the flow field is initialized with

$$(\rho, u, p)_{t=0} = \begin{cases} (3.85714, & 2.629369, & 10.33333) & x \leq -0.8 \\ (1.0 + \epsilon \sin(\kappa\pi x), & 0, & 1.0) & x > -0.8, \end{cases} \tag{32}$$

where ϵ=0.2 and κ=5. FIG. 13(a) and FIG. 13(b) show the solution of the density with 128

and 256 cells, respectively. The 'Exact' solution here is the solution computed by the third-order ENO with 1200 cells. As evident in the solution, the complicated flow field behind the shock is well resolved and the shock remains sharp. However, small oscillations near the shock still exist due to the fact that we do not attempt to locate this shock intentionally. If we predict the position of the shock and apply a local filter near the shock at the final time step, it is believed that more satisfactory results can be obtained.

C. Euler systems in two dimensions

In two dimensions, the Euler equation for gas dynamics in a vector notation takes the conservation form

$$U_t + F(U)_x + G(U)_y = 0 \tag{33}$$

with

$$U = \begin{pmatrix} \rho \\ \rho u \\ \rho v \\ E \end{pmatrix}; \quad F(U) = \begin{pmatrix} \rho u \\ \rho u^2 + p \\ \rho uv \\ u(E+p) \end{pmatrix}; \quad G(U) = \begin{pmatrix} \rho v \\ \rho uv \\ \rho v^2 + p \\ v(E+p) \end{pmatrix}, \tag{34}$$

$$p = (\gamma - 1)(E - \frac{1}{2}\rho(u^2 + v^2)), \tag{35}$$

where (u, v) is the 2D fluid velocity and $\gamma = 1.4$ is used in all computations.

Example 9. As the first example, we use our spectral scheme to study the interaction between a normal shock and a weak entropy wave which makes an angle $\theta \in (0, \pi/2)$ against the x-axis. If $\theta = 0$, we have essentially the 1D problem (see example 7). The initial conditions are defined as follows: the right state of the shock is given as (ρ_r, u_r, v_r, p_r)=(1, 0, 0, 1) with a given shock Mach number $M_s = 3$. We add a small entropy wave to the flow on the right of the shock which is equivalent to changing only the density of the flow on the

right of the shock. In our problem we change the density ρ_r in the right state of the shock by multiplying ρ_ϵ

$$\begin{aligned} \rho &= \rho_r \rho_\epsilon \\ \rho_\epsilon &= e^{-(\epsilon/p_r)\sin(\kappa(x\cos\theta + y\sin\theta))} \end{aligned} \tag{36}$$

with ϵ and κ being the amplitude and wavenumber, respectively. In order to carry out a long time integration and to enforce periodic boundary condition in y-direction, the computational domain is taken to be $[0, 9] \times [0, \frac{2\pi}{\kappa \sin\theta}]$. We initially position the normal shock at $x = 0.5$ and allow it to move up to $x = 8.5$. In our simulation, we adopt $\epsilon = 0.1$, $\kappa = 15$, and $\theta = 30^\circ$. The performance is measured by drawing the maximum amplitudes of the amplified entropy waves in the y-direction for all fixed grid values $x \in [7.4, 8.4]$, and comparing them with the amplitude predicted by the linear analysis, which is 0.08744786.

We use 513 grid points in the x-direction and 32 grid points in the y-direction in our test. In order to avoid peak/valley losses of the entropy waves due to insufficient grid points near these positions, we interpolate our final results to a denser grid when plotting them. FIG. 14 displays the amplitudes of the amplified entropy waves. Obviously, the compressed entropy waves are well resolved in the post-shock regime even though small oscillations remain near the location of the shock. It is believed that such a trivial flaw is acceptable.

This example has further demonstrated the capability of our spectral scheme for capturing small scale waves in the presence of a shock.

Example 10. This model problem describes the interaction between a stationary shock and a vortex. It has many potential applications and has been treated by many researchers using various techniques. Early numerical studies in this area using spectral methods focused primarily on shock-fitting techniques. However, for the cases in which a vortex causes a shock to deform at the point of bifurcation, it is generally difficult for a shock-fitting method to apply. This problem was successfully simulated in Refs. [6,8] by using the Chebyshev spectral method. In this paper, we also adopt this model to access the capability of the proposed spectral shock-capturing method. This problem is defined as follows. The initialization is imposed on the domain $[0, 2] \times [0, 1]$ with a stationary normal shock at $x = 0.5$ and a Mach

1.1 flow at the inlet. The right state of the shock is given as $(\rho_r, u_r, v_r, p_r) = (1, 1.1\sqrt{\gamma}, 0, 1)$. A vortex is generated by a perturbation to the velocity (u, v), temperature T and entropy S which is centered at $(x_c, y_c) = (0.25, 0.5)$ and in the forms

$$u' = \epsilon\tau e^{\alpha(1-\tau^2)} \sin\theta \tag{37}$$

$$v' = -\epsilon\tau e^{\alpha(1-\tau^2)} \cos\theta \tag{38}$$

$$T' = -\frac{(\gamma-1)\epsilon^2 e^{2\alpha(1-\tau^2)}}{4\alpha\gamma} \tag{39}$$

$$S' = 0 \tag{40}$$

where, $\tau = \frac{r}{r_c}$, $r = \sqrt{(x-x_c)^2 + (y-y_c)^2}$ and $\theta = \tan^{-1}((y-y_c)/(x-x_c))$. Here ϵ denotes the strength of the vortex, α is the decay rate of the vortex. Note that we can obtain perturbations in ρ and p according to the relations of $T = p/\rho$ and $S = \ln\frac{p}{\rho^\gamma}$. In our numerical experiment, we choose $\epsilon = 0.3$, $r_c = 0.05$ and $\alpha = 0.204$.

A reflective boundary is imposed on both the upper and lower boundaries. We solve the Euler equations on a 257×129 Cartesian grid, which is uniform in y-direction and refined in x-direction around the shock using the Roberts transformation [2]. Once again, we emphasize that the DSC-RSK lowpass filter is used in the physical domain directly for this problem due to the presence of the reflective boundaries. FIGs. 15(a-e) show a time evolution of shock-vortex interaction in terms of the pressure contours. We can see that even at t=0.8 the solution (FIG. 15(e)) is almost free of oscillations and the fine scale features are captured very well. Particularly, the shock bifurcation reflected on the top boundary is shown clearly.

In order to explore the potential of our algorithm further, we increase the flow Mach number up to 3.0 and the strength of the vortex ϵ up to 0.6. The results at t=0.2 are shown in FIG. 16. Deformation and bifurcation of the shock are observed clearly. These results indicate that the applicability of our spectral shock-capturing scheme is not limited to low Mach number and low vortex strength. Flows of high Mach number and high vortex strength can also be successfully simulated.

Example 11. In this case, we investigate the advection of an isentropic vortex in a free

stream. As the exact solution of this problem is available, it is a good test for examining the accuracy and stability of shock capturing schemes.

Consider a mean flow of $(\rho_\infty, u_\infty, v_\infty, p_\infty, T_\infty) = (1, 1, 1, 1, 1)$ with a periodic boundary condition in both directions. At t_0, the flow is perturbed by an isentropic vortex (u', v', T') centered at (x_0, y_0), having the forms of

$$u' = -\frac{\lambda}{2\pi}(y - y_0)e^{\eta(1-s^2)}, \tag{41}$$

$$v' = \frac{\lambda}{2\pi}(x - x_0)e^{\eta(1-s^2)}, \tag{42}$$

$$T' = -\frac{(\gamma - 1)\lambda^2}{16\eta\gamma\pi^2}e^{2\eta(1-s^2)}. \tag{43}$$

Here, $s = \sqrt{(x - x_0)^2 + (y - y_0)^2}$ is the distance to the vortex center; λ is the strength of the vortex and η is a parameter determining the gradient of the solution. In our test, we choose them as $\lambda = 5$ and $\eta = 1$ unless we further specify. Note that for an isentropic flow, relations $p = \rho^\gamma$ and $T = p/\rho$ are valid. Therefore, the perturbed ρ is required to be

$$\rho = (T_\infty + T')^{1/(\gamma-1)} = \left[1 - \frac{(\gamma - 1)\lambda^2}{16\eta\gamma\pi^2}e^{2\eta(1-s^2)}\right]^{1/(\gamma-1)}. \tag{44}$$

The computational domain is taken to be $[0, 10] \times [0, 10]$ with the center of the vortex being initially located at $(x_0, y_0) = (5, 5)$, the geometrical center of the computational domain.

Since there is no presence of shock in this problem, spectral method on its own can already provide excellent results if the time integration period is small enough. As such, the lowpass filter is not needed in an initial time period. However, as time progresses, errors would accumulate rapidly and the computation could become unstable if the lowpass filter is not activated to efficiently control the dramatically nonlinear growth of the errors. In our numerical experiment which is not shown here, the computation blows up at around t=13 if no filter is used.

Two experiments are conducted in this study. One is to examine the accuracy of our spectral code and the other is to investigate the stability of our scheme for a long time integration. For the first experiment, we compute the solution of ρ at the time t=2 using

three sets of meshes ($N = 32, 64, 128$). To make the spatial error dominant, we optimize the CFL number to be 0.01.

Two error measures, L_1 and L_2, have been used. To be consistent with the literature [11], two errors used in this problem are defined as

$$L_1 = \frac{1}{(N+1)^2} \sum_{i=0}^{N} \sum_{j=0}^{N} |f_{i,j} - \bar{f}_{i,j}| \tag{45}$$

$$L_2 = \frac{1}{(N+1)} \sqrt{\sum_{i=0}^{N} \sum_{j=0}^{N} |f_{i,j} - \bar{f}_{i,j}|^2}, \tag{46}$$

where f is the numerical result and $\bar{f}$ the exact solution. Note that they are not the standard definitions. The errors for the density with respect to the exact solution are listed in Table I in which we also list the results of some other schemes for a comparison. As the table highlights, the accuracy of the Fourier spectral method is comparative to that of the DSC method [48], while both Fourier spectral and DSC methods are much more accurate than the fourth-order accurate, conservative central scheme (C4).

Our next numerical experiment concerns the performance of our spectral code for a long time integration. Here, we compute the solution of ρ at the time t=100, 200, 400, 600, 800 and 1000, with the grid $N = 64$. Note that we choose the gradient of the solution $\eta = 0.5$ in this case. We list the L_1 and L_2 errors for the density in Table II. It can be seen that our spectral code is highly accurate even after such a long time evolution. The results indicate that our spectral scheme together with the DSC lowpass filter is reliable for the numerical approximation of conservation laws.

Example 12. Finally, we consider the problem of a supersonic flow past a cylinder [23]. This example is used to mainly examine the ability of our DSC filter spectral scheme in handling a non-rectangular domain.

The physical domain is on the $x - y$ plane, and the computational domain is chosen to be [0, 1] $\times$ [0, 1] on the $\xi - \eta$ plane. The mapping between the computational domain and the physical domain is

$$
\begin{aligned}
x = & -(R_x - (R_x - 1)\xi)\cos(\theta(2\eta - 1)) \\
y = & \quad (R_y - (R_y - 1)\xi)\sin(\theta(2\eta - 1))
\end{aligned}
\tag{47}
$$

where we take $R_x = 3$, $R_y = 6$ and $\theta = \frac{5\pi}{12}$.

The flow field is initialized with a Mach 3 shock moving from the inlet, i.e., $\xi = 0$, toward the cylinder. The state in front of the shock is given as $(\rho_r, u_r, v_r, p_r) = (1.4, 1.0, 0, 1.0)$. We impose a reflective boundary condition on the surface of the cylinder, i.e., $\xi = 1$, and the outflow boundary condition at $\eta = 0$ and $\eta = 1$. In our simulation, a uniform mesh of 65×129 in the computation domain is used. FIG. 17(a) depicts a diagram of the mesh (drawing every other grid line) in the physical domain. Like the case on a rectangular domain, we double the computational domain in both ξ and η directions when we approximate the first order derivative of the flux using the Fourier spectral method. The numerical result given in terms of pressure contours (obtained at t=4.5) is shown in FIG. 17(b). In summary, our spectral scheme can be easily applied to the nonrectangular domain, as long as the domain can be smoothly transformed to the rectangular one.

IV. CONCLUSION REMARKS

In this work, we introduce the use of discrete singular convolution (DSC) filters in the Fourier pseudospectral method (FPM) for the simulation of hyperbolic conservation law systems. The fast Fourier transform (FFT) is used as the basic scheme, while DSC low-pass filters are used to suppress unphysical oscillations. The DSC filters are implemented in either the Fourier domain or the physical domain, depending on the physical problem under consideration. The Fourier domain implementation is easy and cost efficient, whereas the physical domain implementation allows more flexibility to handle some special boundary conditions. A sensor technique developed in the conjugate filter oscillation reduction (CFOR) scheme [19,45,46] is adopted in the present work to appropriately activate the DSC filter. The fourth-order Runge-Kutta scheme is utilized for the time integration.

Extensive numerical experiments are considered to validate the proposed approach and

to demonstrate its usefulness. Excellent numerical results are obtained for all problems examined. The DSC filters turn out to be very effective in removing the Gibbs oscillations produced by the spectral approximation while maintaining a high accuracy. Moreover, it is also highlighted that these filters can dramatically improve the stability of the spectral method for the long time integration. The main features of proposed method are the follows:
(1) The basic scheme, the FPM is of spectral accuracy, which is important for problems that require not only capturing shock waves, but also resolving fine flow structures.
(2) The use of FFT endows the method high efficience, which is desirable for large scale problems in science and engineering.
(3) Numerical dissipation of the DSC filters is adjustable for a given problem, which endows the proposed method the ability to handle problems that are sensitive to numerical dissipation. The interaction of turbulence and shock is arguably a problem of this kind.
(4) The Fourier domain algorithm can be regarded as a windowed Fourier pseudospectral method for shock-capturing. The alternative use of the DSC filter in the physical domain makes the proposed method feasible to problems requires special boundary conditions, e.g., reflective boundary condition.
(5) The proposed scheme by-passes finding the characteristics which is required in many other shock-capturing schemes.
(6) The use of the method in higher dimensions is straitforward.

It is note that the state of art shock-capturing schemes, such as WENO and central schemes, do not depend on any adjustable parameter. To make the proposed scheme robust and user friendly, future work will focus on developing sophisticated sensors so that the filter parameter will be chosen automatically for each given problem. We believe that this can be accomplished by analyzing the Fourier power spectrum distribution of the approximate solution at selected time steps.

Acknowledgments This work was supported in part by Michigan State University.

REFERENCES

[1] S. Abarbanel, D. Gottlieb and E. Tadmor, Spectral methods for discontinuous problems, in *Numerical Methods for Fluid Dynamics*, (K. Morton and M. Baines eds.), (Oxford University Press, New York, 129-153 1986).

[2] D. A. Anderson, J. C. Tannehill, and R. H. Pletcher, Computational fluid mechanics and heat transfer, (McGraw-Hill, New York, 1984).

[3] F. Bianco, G. Puppo and G. Russo, High-order central differencing for hyperbolic conservation laws, *SIAM J. Sci. Comput.*, **21**, 294-322 (1999).

[4] J. P. Boyd, Chebyshev and Fourier Spectral Methods, (2nd ed. Dover, New York, 2000).

[5] W. Cai, D. Gottlieb and C.-W. Shu, Essentially nonoscillatory spectral Fourier methods for shock wave calculations, *Math. Comp.*, **52**, No. 186, 389-410 (1989).

[6] W. Cai and C.-W. Shu, Uniform high-order spectral methods for one- and two-dimensional Euler equations, *J. Comput. Phys.*, **104**, 427-443 (1993).

[7] C. Canuto, M. Y. Hussaini, A. Quarteroni and T. A. Zang, Spectral methods in fluid dynamics, (Springer-Verlag, Berlin, 1988).

[8] W. S. Don, Numerical study of pseudospectral methods in shock wave applications, *J. Comput. Phys*, **110**, 103-111 (1994).

[9] W. S. Don and D. Gottlieb, Spectral simulation of supersonic reactive flows, *SIAM J. Numer Anal.*, **35**, 2370-2384 (1998).

[10] B. Fornberg, A Practical Guide to Pseudospectral Methods, (Cambridge University Press, Cambridge 1996).

[11] E. Garnier, P. Sagaut and M. Deville, A class of explicit ENO filters with application to unsteady flows, *J. Comput. Phys.*, **170**, 184-204 (2001).

[12] D. Gottlieb, M. Y. Hussaini and S. A. Orszag, Introduction: Theory and Applications of

Spectral Methods, in *Spectral Methods for Partial Differential Equations*, R. G. Voigt, D. Gottlieb and M. Y. Hussaini eds., (SIAM, Philadelphia, 1984).

[13] D. Gottlieb and E. Tadmor, Recovering pointwise values of discontinuous data within spectral accuracy, in *Progress and Supercomputing in Computational Fluid Dynamics*, Earll M. Murman and Saul S. Abarbanel eds., (Birkh äuser, 357-375 1985).

[14] D. Gottlieb, C.-W. Shu, A. Solomonoff and H. Vandeven, On the Gibbs phenomenon I, *J. Comput. Appl. Math.*, **43**, 81-98 (1992).

[15] D. Gottlieb, Issues in the application of high order schemes, in *Algorithmic Trends in Computational Fluid Dynamics*, (Springer-Verlag, New York, 195-218 1993).

[16] D. Gottlieb and C.-W. Shu, On the Gibbs phenomenon and its resolution, *SIAM Review*, **39**, No. 4, 644-668 (1997).

[17] D. Gottlieb and J. S. Hesthaven, Spectral methods for hyperbolic problems, *J. Comput. Appl. Math.*, **128**, 83-131 (2001).

[18] T. Grahs and T. Sonar, Entropy-controlled artificial anisotropic diffusion for the numerical solution of conservation laws based on algorithms from image processing *J. Vis. Commun. Image R.*, **13**, 176-194 (2002).

[19] Y. Gu and G. W. Wei, Conjugated filter approach for shock capturing, *Commun. Numer. Meth. Engng.*, **19**, 99-110 (2003).

[20] A. Harten, B. Engquist, S. Osher and S. Chakravarthy, Uniform high-order accurate essentially non-oscillatory schemes, III, *J. Comput. Phys.*, **131**, 3-47 (1997).

[21] J. S. Hesthaven and D. Gottlieb, Stable spectral methods for conservation laws on triangles with unstructured grids, *Comput. Method Appl. Mech. Engng.*, **175**, 361-381 (1999).

[22] M. Y. Hussaini, D. A. Kopriva, M. D. Salas and T. A. Zang, Spectral methods for the

Euler equation: Part I - Fourier methods and shock-capturing, *AIAA J.*, **23**, No. 1, 64-70 (1985).

[23] G.-S. Jiang and C.-W. Shu, Efficient implementation of weighted ENO schemes, *J. Comput. Phys*, **126**, 202 (1996).

[24] S. Jin and C. D. Levermore, Numerical schemes for hyperbolic conservation laws with stiff relaxation terms, *J. Comput. Phys.*, **126**, 449-467 (1996).

[25] A. Kurganov and D. Levy, A third-order semidiscrete central scheme for conservation laws and convention diffusion equations, *SIAM J. Sci. Comput.* **22**, 1461-1488 (2000).

[26] F. Lafon and S. Osher, Essentially nonoscillatory postprocessing filtering methods, in *Algorithmic Trends in Computational Fluid Dynamics*, (New York : Springer-Verlag, 219-243 1993).

[27] F. Lafon and S. Osher, High order filtering methods for approximating hyperbolic systems of conservation laws, *J. Comput. Phys.*, **172**, 574-591 (1992).

[28] R. J. LeVeque and M. Pelanti, A class of approximate Riemann solvers and their relation to relaxation schemes, *J. Comput. Phys.*, **172**, 574-591 (2001).

[29] X.-D. Liu, S. Osher and T. Chan, Weighted essentially non-oscillatory schemes, *J. Comput. Phys.* **115**, 200-212 (1994).

[30] X.-D. Liu and E. Tadmor, Third order non-oscillatory central scheme for hyperbolic conservation laws, *Numer. Math.*, **79**, 397-425 (1998).

[31] S. Lee, S. K. Lele and P. Moin, Interaction of isotropic turbulence with shock waves: Effect of shock strength, *J. Fluid Mech.*, **340**, 225-247 (1997).

[32] A. Majda, J. McDonough and S. Osher, The Fourier method for nonsmooth initial data, *Math. Comput.*, **32**, No. 144, 1041-1081 (1978).

[33] L. S. Mulholland and D. M. Sloan, The effect of filtering on the pseudospectral solution

of evolutionary partial differential equation, *J. Comput. Phys.*, **96**, 369-390 (1991).

[34] H. Nessyahu and E. Tadmor, Non-oscillation central differencing for hyperbolic conservation laws, *J. Comput. Phys.*, **87**, 408-463 (1990).

[35] J.-X. Qiu and C.-W. Shu, On the construction, comparison, and local characteristic decomposition for high order central WENO schemes, *J. Comput. Phys.*, in press.

[36] C.-W. Shu, Essentially non-oscillatory and weighted essentially non-oscillatory schemes for hyperbolic conservation laws, *ICASE Report*, No. **97-65**, (1997).

[37] E. Tadmor, Convergence of spectral methods for nonlinear conservation laws, *SIAM J. Numer. Anal.*, **26**, 30-44 (1989).

[38] E. F. Toro, R. C. Millington and V. A. Titarev, ADER: arbitrary-order non-oscillatory advection scheme, *Proc. 8th International Conference on Non-linear Hyperbolic Problems*, (Magdeburg, Germany, March, 2000).

[39] L. N. Trefethen, Spectral Methods in Matlab, (Oxford University, Oxford, England, 2000).

[40] H. Vandeven, Family of spectral filters for discontinuous problems, *J. Sci. Comput.*, **6**, 159-192 (1991).

[41] D. C. Wan, B. S. V. Patnaik and G. W. Wei, Discrete singular convolution-finite subdomain method for the solution of incompressible viscous flows, *J. Comput. Phys.*, **180**, 229-255 (2002).

[42] G. W. Wei, Discrete singular convolution for the solution of the Fokker-Planck equations, *J. Chem. Phys.*, **110**, 8930-8942 (1999).

[43] G. W. Wei, Y. B. Zhao and Y. Xiang, Discrete singular convolution and its application to the analysis of plates with internal supports. I. Theory and algorithm, *Int. J. Numer. Meth. Engng.*, **55**, 913-946 (2002).

[44] G. W. Wei, Oscillation reduction by anisotropic diffusions, *Comput. Phys. Commun.*, **144**, 317-342 (2002).

[45] G. W. Wei, and Y. Gu, Conjugated filter approach for solving Burgers' equation, *J. Comput. Appl. Math.*, **149**, 439-456 (2002); arXiv:math.SC/0009125, Sept. 13, (2000).

[46] Y. C. Zhou and G. W. Wei, High resolution conjugate filters for the simulation of flows, preprinter.

[47] K. Xu, A gas-kinetic BGK scheme for the Navier-Stokes equations and its connection with artificial dissipation and Godunov method, *J. Comput. Phys.*, **171**, 289-335 (2001).

[48] S. Y. Yang, Y. C. Zhou, and G. W. Wei, Comparison of the discrete singular convolution algorithm and the Fourier pseudospectral method for solving partial differential equations, *Comput. Phys. Commun.*, **143**, 113-135 (2002).

[49] H. C. Yee, N. D. Sandham and M. J. Djomehri, Low-dissipative high-order shock-capturing methods using characteristic-based filters, *J. Comput. Phys.* **150**, 199-238 (1999).

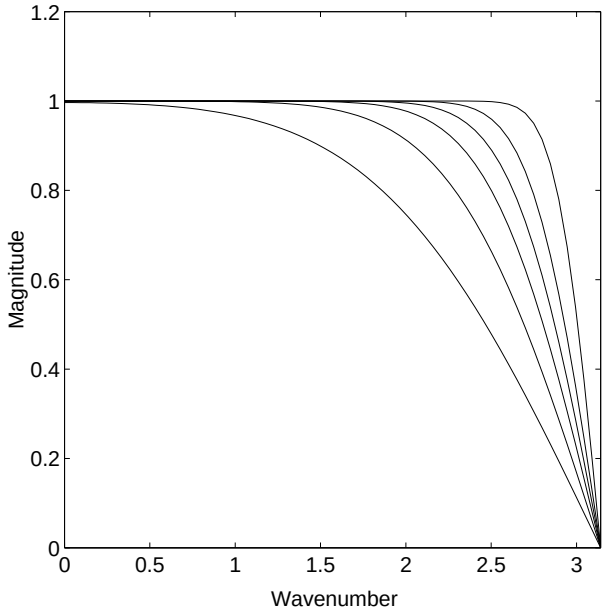

FIG. 1. Magnitude response of the DSC-RSK filter. $r = 1.0, 1.5, 2.0, 2.5, 3.2, 5.0$ from the left to right.

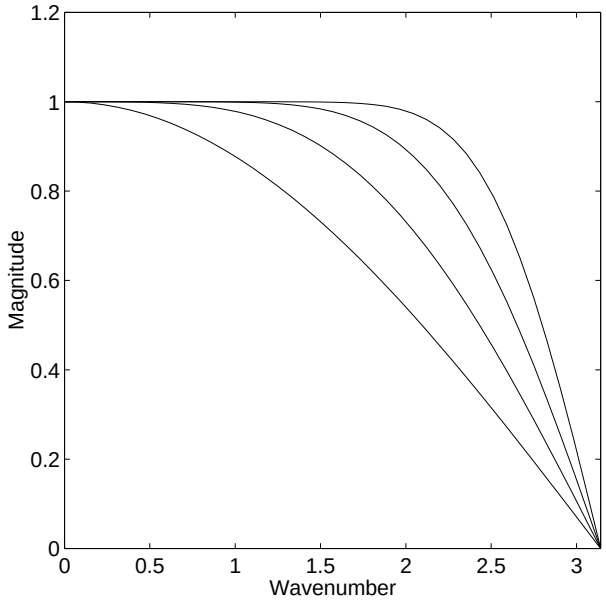

FIG. 2. Magnitude response of the Lagrange filter. Lagrange-2, Lagrange-4, Lagrange-8 and Lagrange-16 from the left to right.

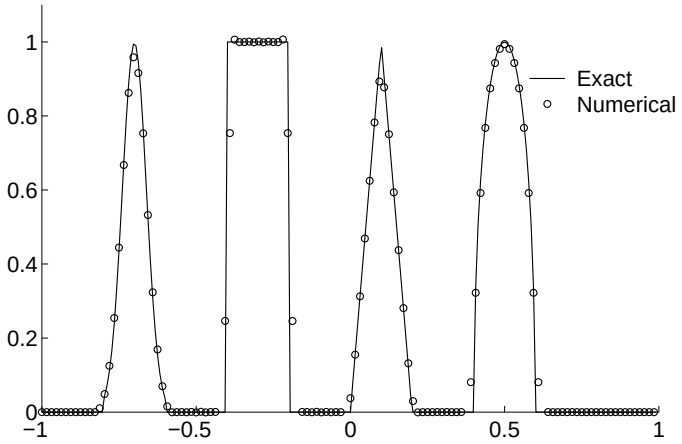

FIG. 3. Linear advection equation. t=8, Δt=0.001, 128 grid points.

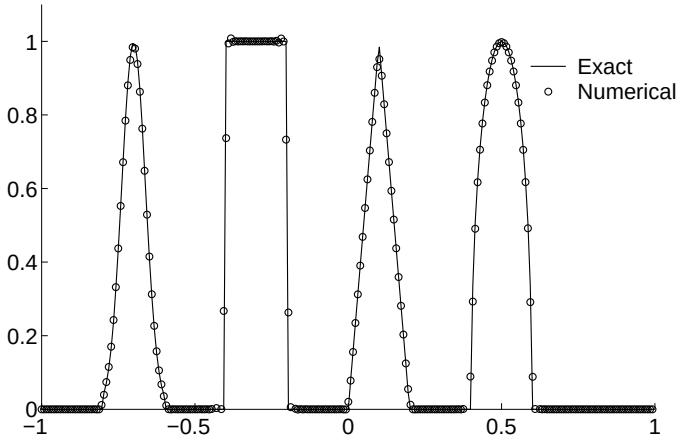

FIG. 4. Linear advection equation. t=8, Δt=0.001, 256 grid points.

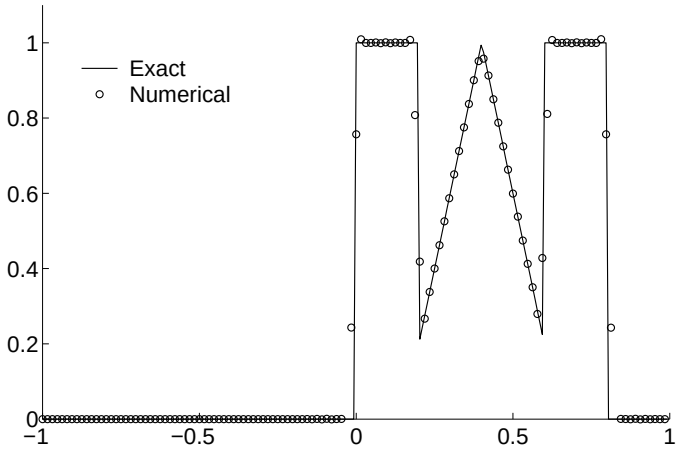

FIG. 5. Linear advection equation. t=8, Δt=0.001, 128 grid points.

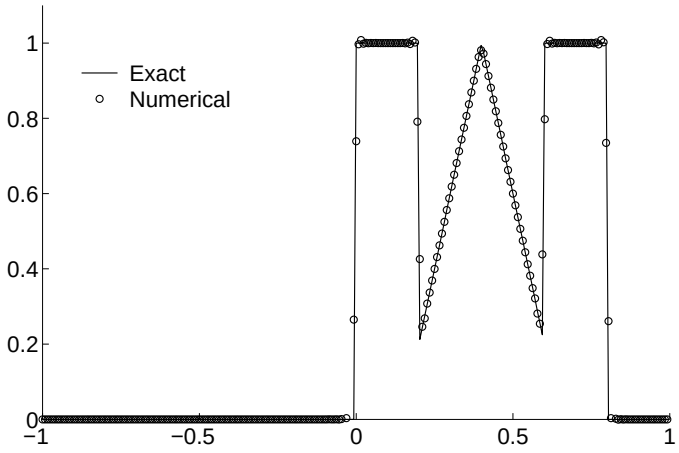

FIG. 6. Linear advection equation. t=8, Δt=0.001, 256 grid points.

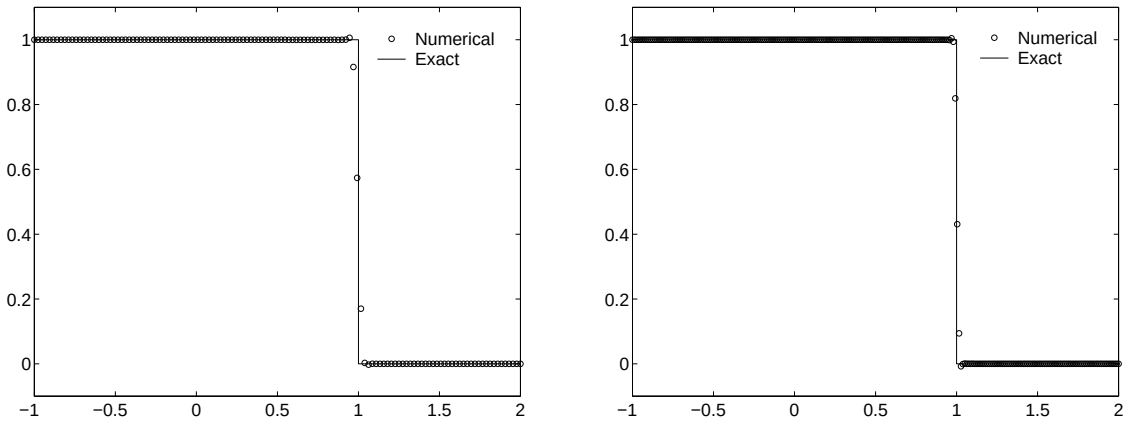

(a) (b)

FIG. 7. Inviscid Burgers' equation (t=2, Δ t=0.005). (a) 129 grid points; (b) 257 grid points.

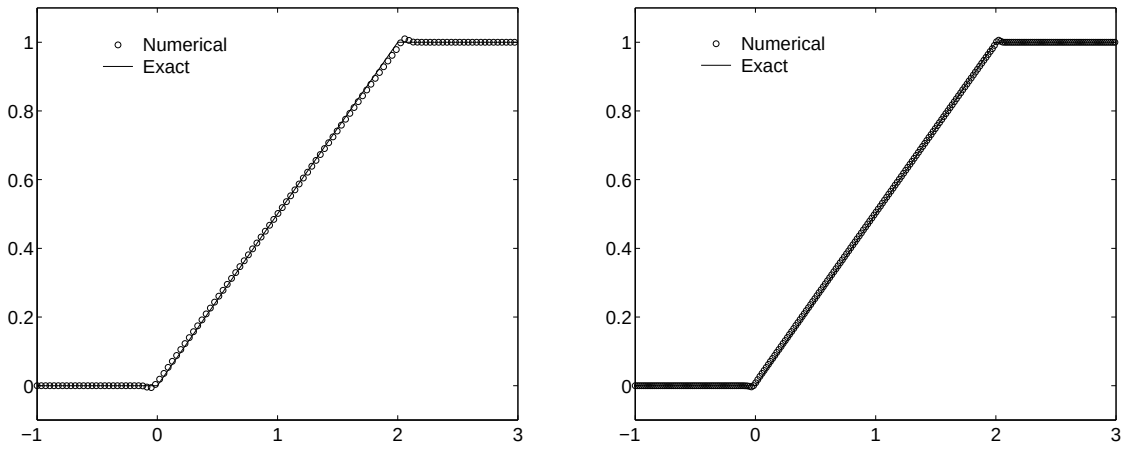

(a) (b)

FIG. 8. Inviscid Burgers' equation with rarefaction wave (t=2, Δt=0.005). (a) 129 grid points; (b) 257 grid points.

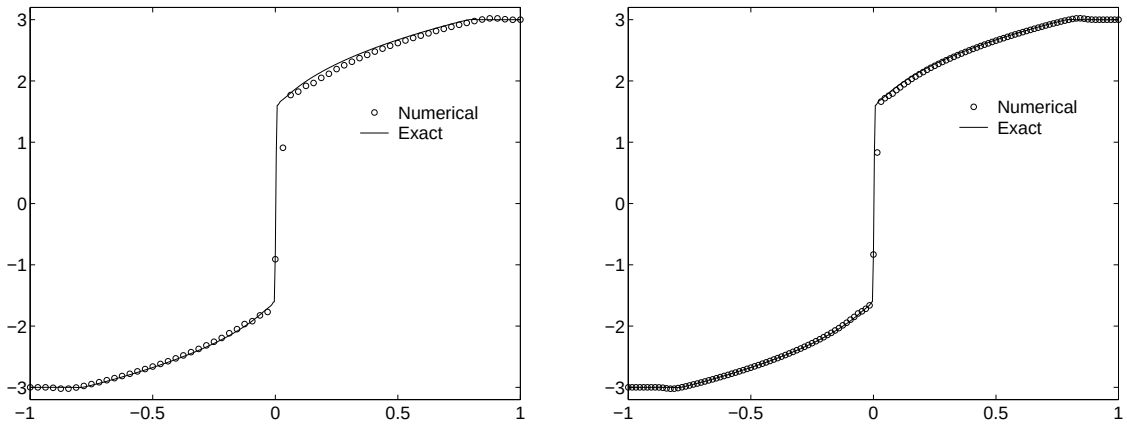

(a) (b)

FIG. 9. Inviscid Burgers' equation with non-convex flux (t=0.04, Δt=0.0005). (a) 65 grid points; (b) 129 grid points.

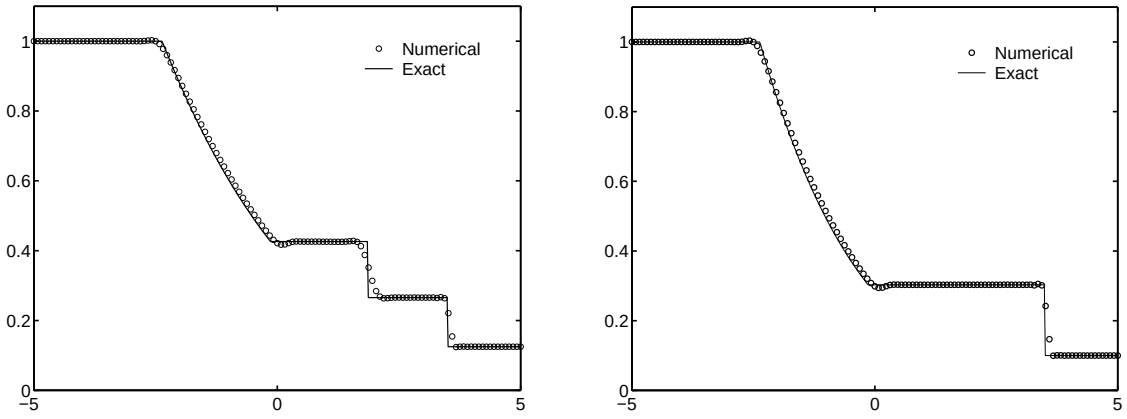

(a) (b)

FIG. 10. Sod's problem (t=2, Δt=0.02, 129 grid points). (a) Density; (b) Pressure.

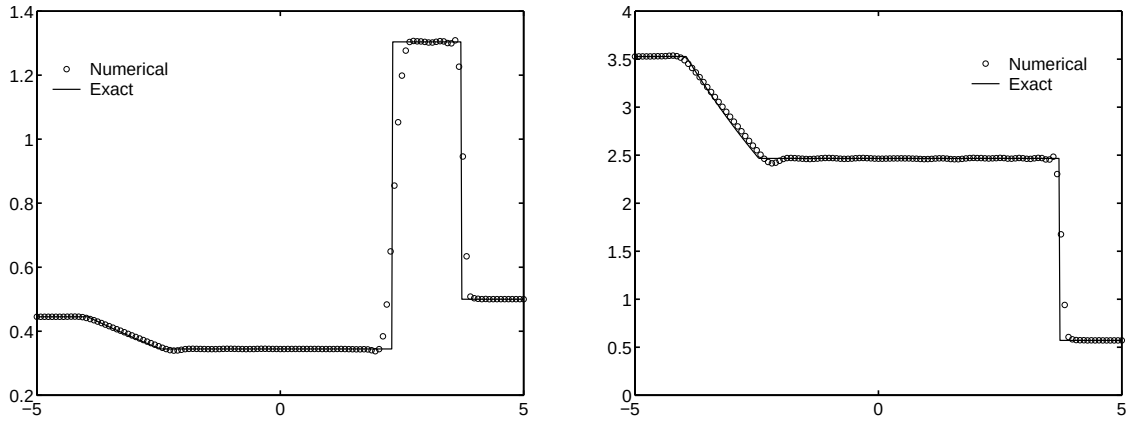

(a) (b)

FIG. 11. Lax's problem (t=1.5, Δt=0.02, 129 grid points). (a) Density; (b) Pressure.

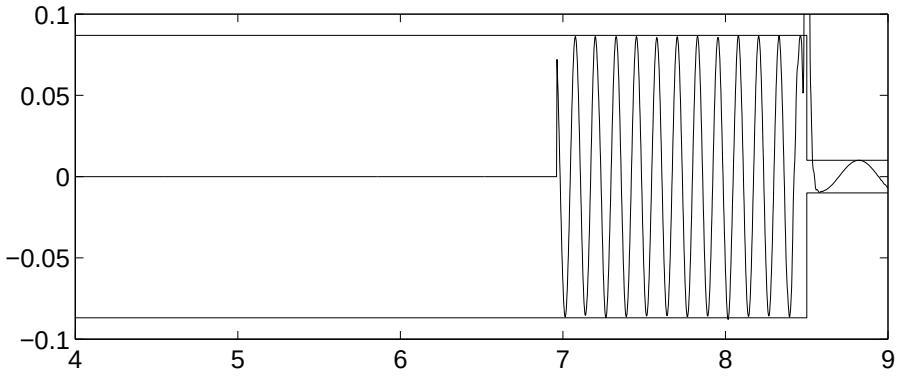

(a) $\kappa = 13$, $N = 513$

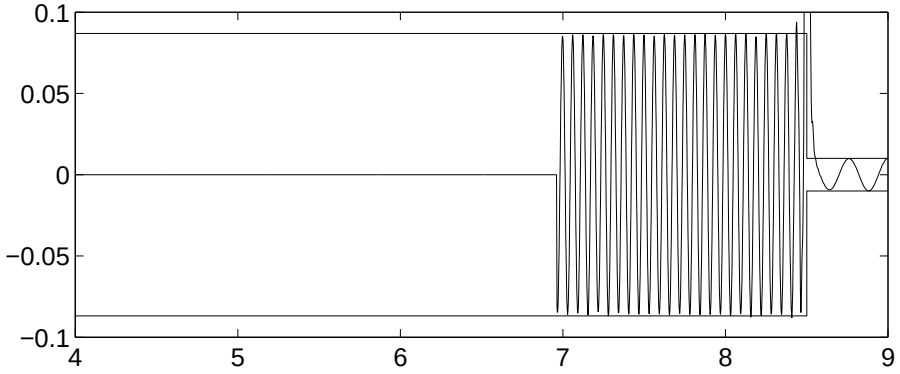

(b) $\kappa = 26$, $N = 1025$

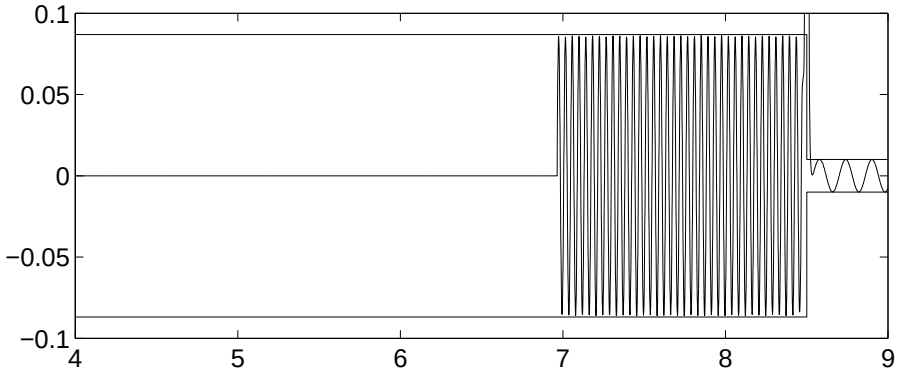

(c) $\kappa = 39$, $N = 2049$

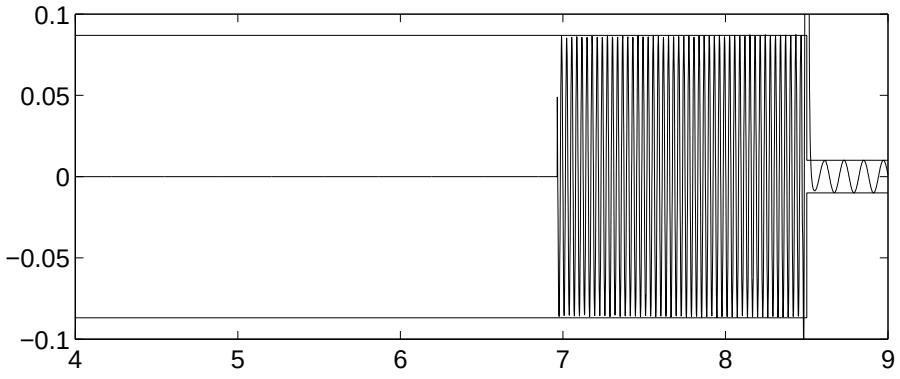

(d) $\kappa = 52$, $N = 2049$

FIG. 12. 1D shock entropy wave interaction. Amplitude of entropy waves.

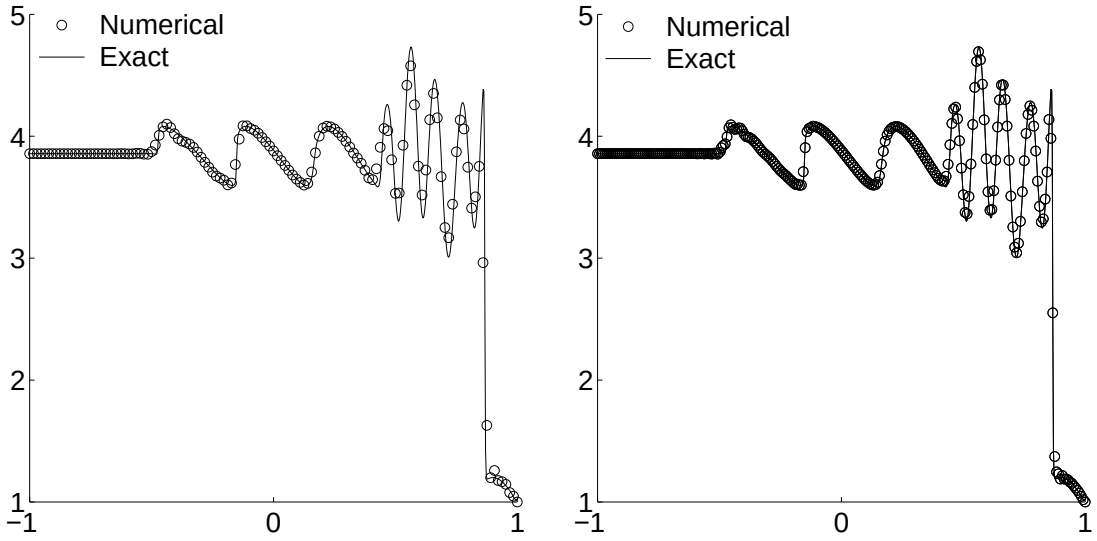

(a) (b)

FIG. 13. Shu-Osher problem (t=0.47). (a) 128 cells; (b) 256 cells.

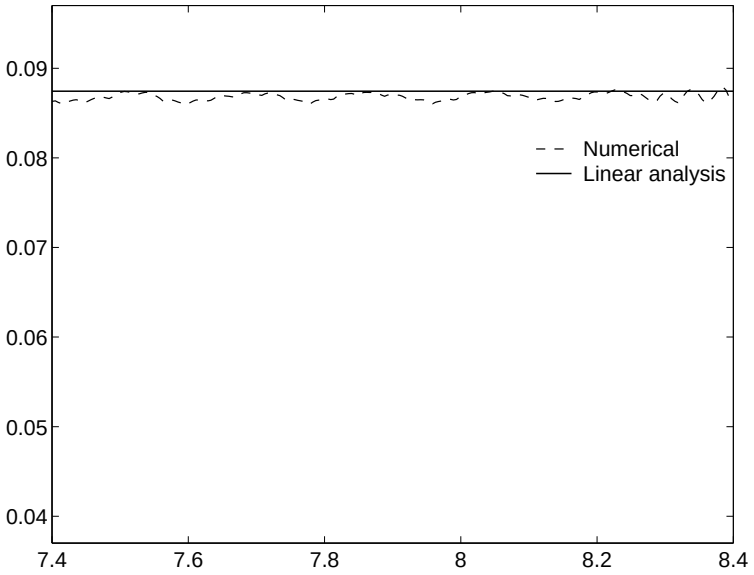

FIG. 14. 2D shock entropy wave interaction ($N = 513$). Amplitude of entropy waves.

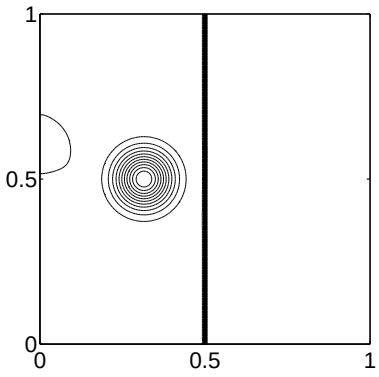

(a) t=0.05, 30 contours

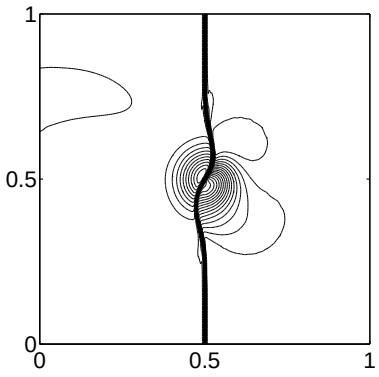

(b) t=0.20, 30 contours

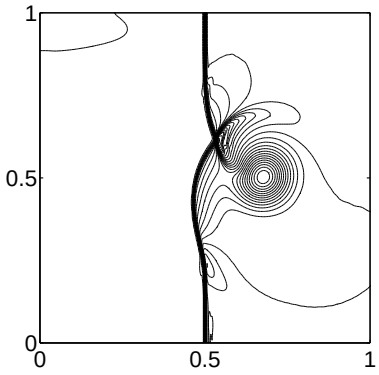

(c) t=0.35, 30 contours

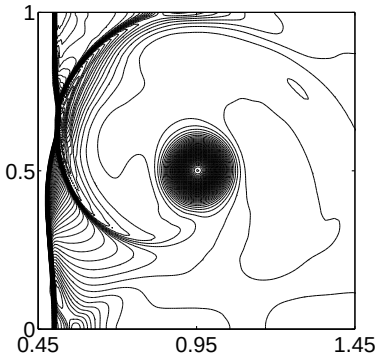

(d) t=0.60, 90 contours from 1.01 to 1.37

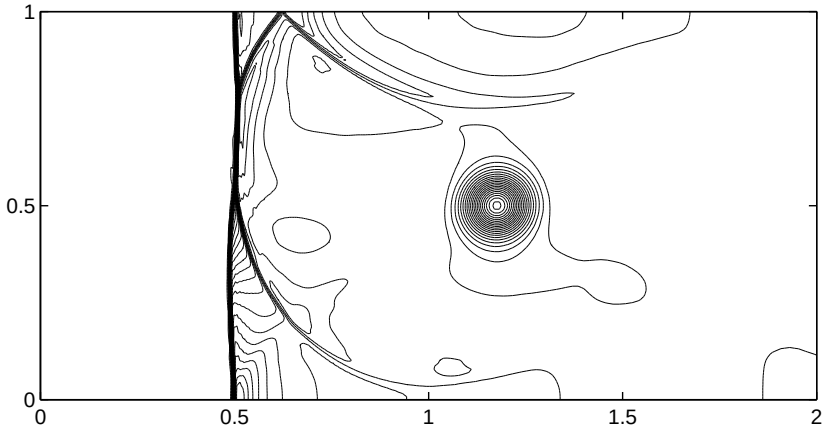

(e) t=0.80, 30 contours from 1.01 to 1.29

FIG. 15. 2D shock vortex interaction (Mach=1.1, $\epsilon = 0.3$, CFL=0.5). Pressure profiles.

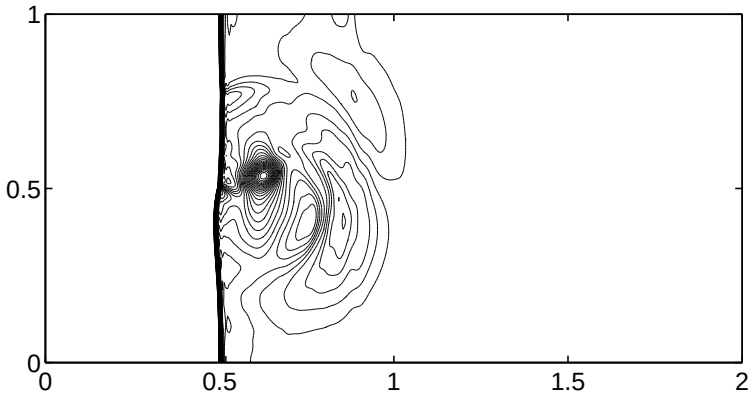

FIG. 16. 2D shock vortex interaction (t=0.2, Mach=3.0, $\epsilon = 0.6$, CFL=0.5). Pressure profiles.

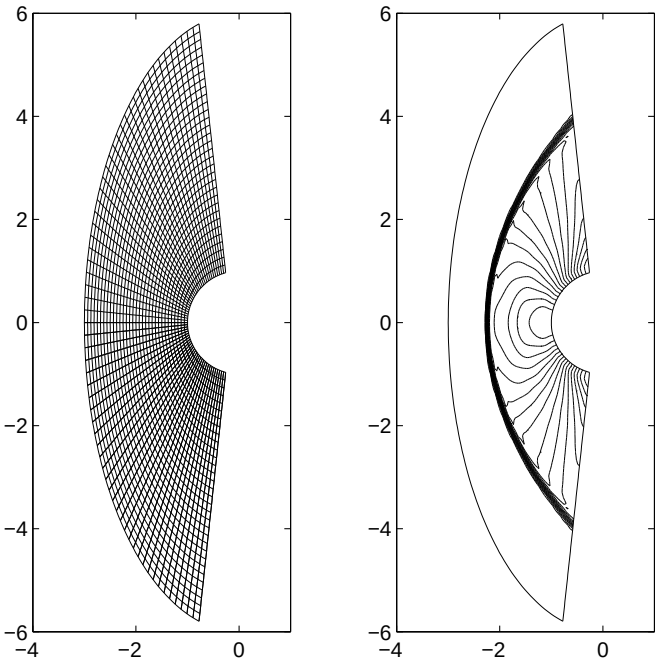

(a) (b)

FIG. 17. Flow pass a cylinder. (a) Physical grid; (b) Pressure with 20 contours.

TABLES

mesh	error	FFT	C4	DSC
N=32	L_1	5.58E-5	1.96E-3	1.27E-4
	L_2	1.27E-4	5.67E-3	4.07E-4
N=64	L_1	2.33E-8	1.32E-4	8.18E-8
	L_2	7.94E-8	4.39E-4	4.07E-7
N=128	L_1	4.01E-11	8.90E-6	3.99E-11
	L_2	5.09E-10	2.96E-5	5.09E-10

TABLE I. Advective 2D isentropic vortex. L_1 and L_2 errors for the density at t=2. The CFL number is 0.01 for all schemes. C4 denotes the fourth-order accurate, conservative centered scheme.

mesh	error	t=100	t=200	t=400	t=600	t=800	t=1000
N=64	L_1	4.63E-7	5.05E-7	1.00E-6	1.44E-6	2.07E-6	2.77E-6
	L_2	1.99E-6	1.23E-6	2.90E-6	4.42E-6	6.02E-6	7.59E-6

TABLE II. Advective 2D isentropic vortex. L_1 and L_2 errors for the density at different times with N=64 (CFL=0.5, η=0.5).

APPENDIX

The optimal values (r) for DSC-RSK lowpass filters in our numerical experiments.

No. of Example	case	r
1	N=128	0.6
	N=256	0.8
2	N=128	0.6
	N=256	0.8
3	N=129	0.7
	N=257	0.8
4	N=129	0.6
	N=257	0.6
5	N=65	0.8
	N=129	0.8
6	Lax	0.95
	Sod	1.1
7	κ=13	2.0
	κ=26	2.0
	κ=39	2.1
	κ=52	2.1
8	N=129	2.0
	N=257	2.1
9		2.1
10		2.8
11	η=1.0	3.2
	η=0.5	2.8
12		1.2